INSTITUT DE FRANCE
Académie des sciences

Comptes Rendus
Chimie

Sonia Cherif, Pierre Bonnet, Lawrence Frezet, Abdoulaye Kane, Aymen Amine Assadi, Mohamed Trari, Hynda Yazid and Hayet Djelal

The photocatalytic degradation of a binary textile dyes mixture within a new configuration of loop reactor using ZnO thin film-phytotoxicity control

Volume 25, Special Issue S3 (2022), p. 261-279

Published online: 4 July 2022

https://doi.org/10.5802/crchim.198

Part of Special Issue: Active site engineering in nanostructured materials for energy, health and environment

Guest editors: Ioana Fechete (Université de Technologie de Troyes, France) and Doina Lutic (Al. I. Cuza University of Iasi, Romania)

Les Comptes Rendus. Chimie *sont membres du Centre Mersenne pour l'édition scientifique ouverte*
www.centre-mersenne.org
e-ISSN : 1878-1543

Comptes Rendus
Chimie
2022, Vol. 25, Special Issue S3, p. 261-279
https://doi.org/10.5802/crchim.198

Active site engineering in nanostructured materials for energy, health and environment / *Ingénierie de sites actifs dans les matériaux nanostructurés pour l'énergie, la santé et l'environnement*

The photocatalytic degradation of a binary textile dyes mixture within a new configuration of loop reactor using ZnO thin film-phytotoxicity control

Sonia Cherif [*, a, b], **Pierre Bonnet** [c], **Lawrence Frezet** [c], **Abdoulaye Kane** [b], **Aymen Amine Assadi** [d], **Mohamed Trari** [e], **Hynda Yazid** [a] **and Hayet Djelal** [b]

[a] Laboratory of Reaction Engineering, Faculty of Mechanical Engineering and Process Engineering, USTHB, BP 32 Al Alia, 16111 Algiers, Algeria

[b] UniLaSalle-Ecole des Métiers de l'Environnement, Cyclann, Campus de Ker Lann, 35 170 Bruz, France

[c] Universite Clermont Auvergne, Institut de Chimie de Clermont-Ferrand (ICCF), 24 Avenue Blaise Pascal, 63178, Aubiere, France

[d] Univ Rennes, Ecole Nationale Supérieure de Chimie de Rennes, CNRS, ISCR, UMR6226, F-35000 Rennes, France

[e] Laboratory of Storage and Valorization of Renewable Energies, Faculty of Chemistry, USTHB, BP 32, El Alia, 16111, Algiers, Algeria

E-mails: cherif14sonia@hotmail.com (S. Cherif), pierre.m.bonnet@uca.fr (P. Bonnet), Lawrence.FREZET@uca.fr (L. Frezet), Abdoulaye.KANE@unilasalle.fr (A. Kane), aymen.assadi@ensc-rennes.fr (A. A. Assadi), solarchemistry@gmail.com (M. Trari), Yazhyn1@yahoo.fr (H. Yazid), Hayet.DJELAL@unilasalle.fr (H. Djelal)

Abstract. ZnO thin film were deposited by Spray and Spray Pyrolysis methods on glass substrates at 370 °C. The structural characterization by XRD, Raman spectroscopy, FTIR, EDS, TEM, SEM, RPE and XPS revealed the purity of ZnO Wurtzite variety in both samples. The use of a new loop reactor configuration for the photocatalytic activity was evaluated against/with respect to the degradation of two textile dyes as well as their binary mixture. The ZnO thin film prepared by Spray Pyrolysis kept its photocatalytic properties even after 20 reuse cycles (148 h). The treated solution showed better biodegradability and the absence of phytotoxicity.

Keywords. Photocatalytic reactor, Characterization ZnO thin film, Synthetic dyes, Photo-stability, Phytotoxicity.

Published online: 4 July 2022

* Corresponding author.

1. Introduction

The industrial wastewater treatment is one of the most important environmental issues that researchers all over the world have to address. The textile industry generates a huge amount of waste water that is loaded by organic and toxic compounds, which are strongly colored [1]. These characteristics make them harmful for both human and aquatic lives [2]. In fact, industrial effluents must be treated before they are discharged in aquatic systems [3].

There are many processes for wastewater pollution abatement, like adsorption, biological treatment, filtration, coagulation flocculation. However, these methods have many inconveniences among which expensiveness and the generation of large amounts of sludge [4,5]. In this respect, Advanced oxidation processes (AOPs) have gained the attention of researchers since the 70's, for their ability to remove pollutants from contaminated water and achieve the mineralization step without generating any sludge [6–8].

Recently, the photocatalysis use for the treatment of a variety of pollutants such as dyes, pesticides, pharmaceuticals and various endocrine disrupting compounds, is rapidly increasing. Photocatalysis refers to the photogeneration of strong oxidizing and reducing agents at the surface of the catalyst that destroy mainly organic pollutants [9, 10]. In this regard, researchers have turned their attention to producing economically viable, nontoxic, stable and photo-corrosion resistant catalysts [11–13].

Various semiconductors have been utilized for the photocatalytic removal of pollutants among which, titanium dioxide (TiO_2) and zinc oxide (ZnO) with a similar band gap (3.2 eV), that are the most widely used as photocatalysts [14]. Although TiO_2 is universally known as the most photoactive catalyst, many reports have outlined the potency of ZnO for the removal of recalcitrant matter [15]. These catalysts can be employed either in a colloidal or an immobilized form. When the particles are dispersed in the aqueous phase, the depth of the radiation penetration is limited due to absorption or scattering by the dissolved organic species and the catalyst particles [16,17]. The primary aim of using the immobilized form is that the costly and extra final filtration process can be avoided, which is important especially for the water decontamination and the catalysts reusability [18]. The supports of the catalyst have to be inert, resistant to erosion and corrosion and possess a large surface area with the capability to keep the catalyst immobilized; in such a way, the catalyst particles do not get unattached from the support and act as suspended catalysts [19,20]. Many supports of ZnO photocatalyst have been studied in literature (Table 1).

The glass plate was selected as substrate for ZnO immobilization in this study. The preference of this support goes to its inertness coupled with its ability to withstand high calcination temperatures, its availability, chemical stability, nontoxicity and low cost [28,29].

Various techniques have been employed to achieve the immobilization of ZnO on the glass plates (Table 2).

Even if extensive research has been conducted on the photodegradation of pollutants, the large-scale applications of this technique are still restricted due to the use of batch reactors. The other reason is credited to the slow evolution of practical photocatalytic systems [24]. Therefore, particular focus/attention must be accorded to the configuration of photocatalytic reactors to promote these processes [37]. The stability of the catalyst film and its successive reuse along with the increased time of the treatment has always remained one of the major concerns in these types of reactors [38]. To improve the photocatalytic efficiency of semiconductors, the UV/H_2O_2/semiconductor system is recommended because of its high tendency to form a substantial amount of reactive oxygen species, which are the basic reactive intermediates needed to facilitate the catalytic process [39,40].

This work aims at: (i) the comparison of ZnO deposited by two methods on glass plates for the removal of two textiles dyes i.e. Reactive Blue 19 and Direct Red 227 in single and binary systems by the photocatalytic process; (ii) the use of a new loop reactor configuration for the photodegradation experiments; (iii) the reusability and stability studies of the immobilized ZnO for practical applications; (iv) the assessment of the biodegradability and the phytotoxicity of the treated solution, which still remains scarcely examined in the literature. It is highly significant to note that very few studies have been carried out using Direct Red 227 dye.

Table 1. Examples of supports used in research for ZnO photocatalyst

Photocatalyst	Support	Pollutant	Initial concentration of pollutant ($mg{\cdot}L^{-1}$)	Degradation yield (%)	Treatment duration (min)	Reference
ZnO	PMMA polymer	Methylene Blue dye	2.5	60	15 h	[21]
Flower-like ZnO hollow microspheres	Flexible ceramic mesh	Cr(VI)	250	86	180	[22]
ZnO nanoparticles	Montmorillonite (MMT)	Metronidazole (antibiotic)	40	97	30	[23]
ZnO	Commercial zeolite	Caffeine	25	100	120	[24]
ZnO	Stones	Acid red 18 dye	25	97	40	[25]
ZnO	Fine pineapple leaf fiber (PALFs)	Congo red dye	20	95	300	[26]
ZnO	Glass plate	*p*-nitroaniline	10	96	105	[27]

Table 2. Immobilization techniques for ZnO NPs on the glass plates

Photocatalyst	Method of fixation	Pollutant	Initial concentration ($mg{\cdot}L^{-1}$)	Degradation yield (%)	Treatment duration (min)	Reference
ZnO	Heat attachment method	Benzene and toluene	50 for benzene and toluene respectively	46% and 57% removal of benzene and toluene respectively	240	[30]
ZnO	Pulsed laser deposition (PLD)	Rhodamine B (RhB) dye	Not reported	91	360	[31]
ZnO	Spin coating	Rhodamine-B (RhB) dye	10.0	93	240	[32]
TiO_2–ZnO	Sole gel dip-coating	Methylene blue	10.0	97	360	[33]
ZnO	Ultrasonic spray pyrolysis technique (USP)	Methylene blue	8.0	99	180	[34]
(Ni) doped ZnO	Chemical bath deposition (CBD)	Methylene blue	3.20	96	150	[35]
ZnO/graphene	One-step electrochemical deposition (ECD)	Methylene blue	Not reported	100	180	[36]

2. Material and methods

2.1. *Chemical products*

Zinc acetate ($(CH_3COO)_2Zn{\cdot}2H_2O$) was purchased from Merck with a purity of 99%. The studied pollutants are two textile dyes namely Reactive Blue 19 (RB19) and Direct Red 227 (DR227). The former Reactive Blue 19 (RB19) dye was purchased from the brand ACROS Organics. This dye was selected because it is considered a model dye of the anthraquinone family. It is a hazardous dye for aquatic mediums. The second dye that is the subject of this study is Direct Red 227 (DR227) dye which was obtained from a textile industry TEXALG that is located in Boufarik, Blida, Algeria. Their characteristics are presented in Table 3.

2.2. *Fixation of ZnO on the glass substrate*

Two simple and economic routes were used to deposit the two thin films of ZnO, which were fixed on glass plates by two methods: “Spray Pyrolysis” and

Table 3. Characteristics of RB19 and DR227 dyes

Trade name	Remazol Blue brilliant R	Solophenyl Red 7BE
Scientific nomenclature	Reactive Blue 19	Direct Red 227
Molecular structure	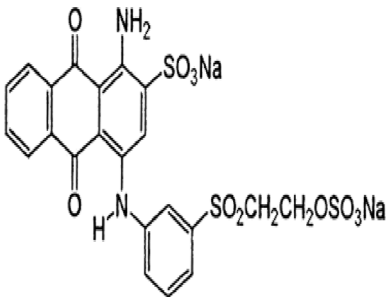	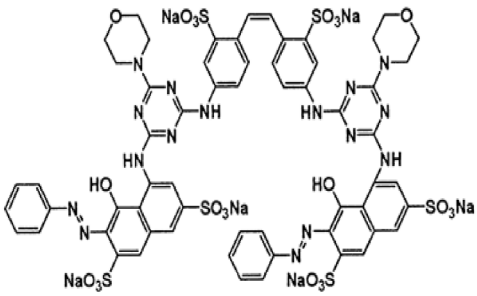
Molecular formula	$C_{22}H_{16}N_2Na_2O_{11}S_3$	$C_{60}H_{46}N_{16}Na_6O_{22}S_6$
Type of structure	Anionic	Anionic
λ_{max} (nm)	593	542
Molecular weight (g·mol^{-1})	626.533	1673.430

"Spray". Osmosis water was used as a solvent for the preparation of all the solutions. All films were immobilized on microscopic glass slides (2.6 cm × 7.6 cm), which were previously rinsed with osmosis water and dried at ambient temperature. A manual aerosol vaporizer was used to spray the solutions on the substrate. The two thin films were prepared under the same conditions to enable the comparison of their photocatalytic efficiency.

2.2.1. *Fixation of ZnO by Spray Pyrolysis*

40 g·L^{-1} of zinc acetate ($(CH_3COO)_2Zn{\cdot}2H_2O$) was dissolved in osmosis water. The glass plate was preheated to 370 °C. 15 ml of Zinc acetate solution was sprayed on the glass plate. A distance of 30 cm was kept between the manual aerosol spray and the substrate glass. The time interval between each spray was 45 s.

2.2.2. *Fixation of ZnO by Spray*

40 g·L^{-1} of ZnO nanoparticles (prepared previously by one step calcination at 420 °C, the synthesis protocol is well-described in Cherif *et al.* [41]) were homogenized in osmosis water under stirring for 3 h, then, the solution was sonicated for 2 h in the ultrasound bath (VWR USC-1). Furthermore, 15 mL of ZnO solution was sprayed on the preheated glass under the same conditions of the Spray Pyrolysis method.

2.3. *Characterization*

The crystalline nature and phase formation of ZnO films were known using the PANAlytical Xpert-PRO diffractometer (Cu-radiation, λ = 1.5406 Å). The Raman spectroscopy using a Jobin Yvon T64000 spectrometer (λ = 514.5 nm; 2.41 eV) in a confocal microscopy mode in air at room temperature, was applied to examine the structural properties of ZnO films. The presence of hydroxyl groups and other inorganic or organic contaminants in the ZnO sample was investigated by Fourier-transform infrared spectroscopy (FT-IR) Nicolet 5700 Fourier spectrometer in the frequency range 4000–400 cm^{-1} with a scan number of 80 and a resolution of 4 cm^{-1}.

The morphology and the size distribution of the prepared powders were analyzed by Scanning Electron Microscopy (SEM, JEOL 5910 LV), and Transmission Electron Microscopy (TEM, Hitachi H-7650) at 80 kV acceleration voltage with magnifications up to 200,000×, the samples investigated by TEM were suspended in ethanol and dropped onto a 400-mesh holey carbon-coated copper grid and dried at room temperature in air. Energy Dispersive X-ray photoelectron spectroscopy analysis (EDX) was taken with a SDD Bruker analyzer.

The Electron Paramagnetic Resonance (EPR) is effective for the detection of vacancies and interstitial defects in metal oxide materials. Thus, it was used for further analyses of the samples, The EPR investiga-

tion was carried out on a Bruker EMX spectrometer in 5 mm diameter quartz tubes using an X Band spectrometer operating at 9.653 GHz, in a resonant cavity ER 4105 DR.

XPS: X-ray photoelectron spectroscopy (XPS) analyses were carried out/conducted using the Omicron brand EA 125 model with a DAR 400 X source. The previously mentioned analysis utilizes the MgKα anode (E = 1253.6 eV) and a hemispheric analyzer working at constant energy of 20 eV for the acquisition of higher solution spectra. A high-resolution measurement was made for Zn2p, O1s, and C1s peaks.

2.4. *Photocatalytic experiments*

The adsorption and photocatalytic experiments of the as-prepared ZnO thin films were assessed by the photodegradation of single RB19 and DR227 (10 mg·L^{-1}) solutions and their binary mixture (5 mg·L^{-1} each) in a loop plexiglass reactor, which had a spherical shape (Figure 1a, b). UV lamp were used as light source, LED type, emitting at 365 nm (Lot:239312/BIN:M.UO). The lamps were placed above the reactor, the effluent to be treated was recirculated using a peristaltic pump. The samples to be analyzed were taken during the photodegradation reaction in the buffer tank. The overall reaction volume Vr was equal to 50 ml. Agitation was carried out mechanically by a magnetic bar. The entire reactor was covered in order to protect the reaction medium from external light.

The flow in the reactor was fixed at 0.06 L·min^{-1}. The assays of the photocatalytic degradation were conducted in room temperature. The dyes solutions were kept in the dark for 60 min within the loop reactor to ensure the adsorption/desorption equilibrium between the dye and the catalyst films, then the UV lamps were turned on. The liquid film thickness in the reactor was 0.38 mm calculated from the following equations:

$$\text{Thickness film} = \left(\frac{\Gamma^2}{g}\right)^{1/3} \tag{1}$$

where:

$$\Gamma = \frac{Q}{L} \tag{2}$$

Γ is the flow rate per unit length (m^3·s^{-1}·m^{-1}), L is the length of the glass plate, Q is the flow rate (m^3·s^{-1}) and g is the gravity (m·s^{-2}). The energy supplied by the lamp is 6.375×10^{-19} $J = 3.41$ eV,[1] which is much higher than that of the band gap of $ZnO_{Spray} = 3.13$ eV and $ZnO_{Spray\ Pyrolysis} = 2.99$ eV (see Section 3.1.1), indicating that the energy provided by the lamp is sufficient for the photocatalytic reaction to take place. The average mass deposited on the glass plate was 3.15×10^{-3} and 2.97×10^{-2} g·cm^{-2} for the thin film prepared by "Spray Pyrolysis" and "Spray" respectively.

2.5. *Reusability and photo-stability of the catalyst for the treatment of binary dyes mixture*

The reusability experiments of ZnO fixed by Spray Pyrolysis were studied by washing the glass plate with osmosis water overnight and drying it at room temperature for few minutes. This plan of regeneration was repeated after each cycle in order to remove the unreacted binary dyes mixture and the byproducts of the previous experiments. This regeneration technique is simple, economic and efficient.

2.6. *Analytical methods*

The samples were analyzed using UV/Vis spectrophotometer (SHIMADZU UV-1800). The concentrations of the two dyes were deduced from the calibration curve. The kinetic constant rates K (min^{-1}) of the two single dyes (RB19/DR227) solutions were calculated using (3)

$$K * t = -Ln\left(\frac{C_t}{C_0}\right) \tag{3}$$

where: C_t is the concentration at the instant t, and C_0 is the initial concentration.

In order to simulate a real textile effluent and examine the performance of the as-prepared thin films on the decomposition of dyes mixture, the photodegradation study was realized on the binary dyes mixture (RB19+DR227). The degradation efficiency of the mixture of the two dyes was calculated from the maximum absorbance of the mixture at 550 nm

[1] $E = hc/\lambda$

where E: is the proton energy in joules (J), h is the Planck's constant (6.63×10^{-34} J·s), c is the speed of light (3×10^8 m/s) and λ is the wavelength in nanometers (nm)

1 electronvolt (eV) = 1.6×10^{-19} J.

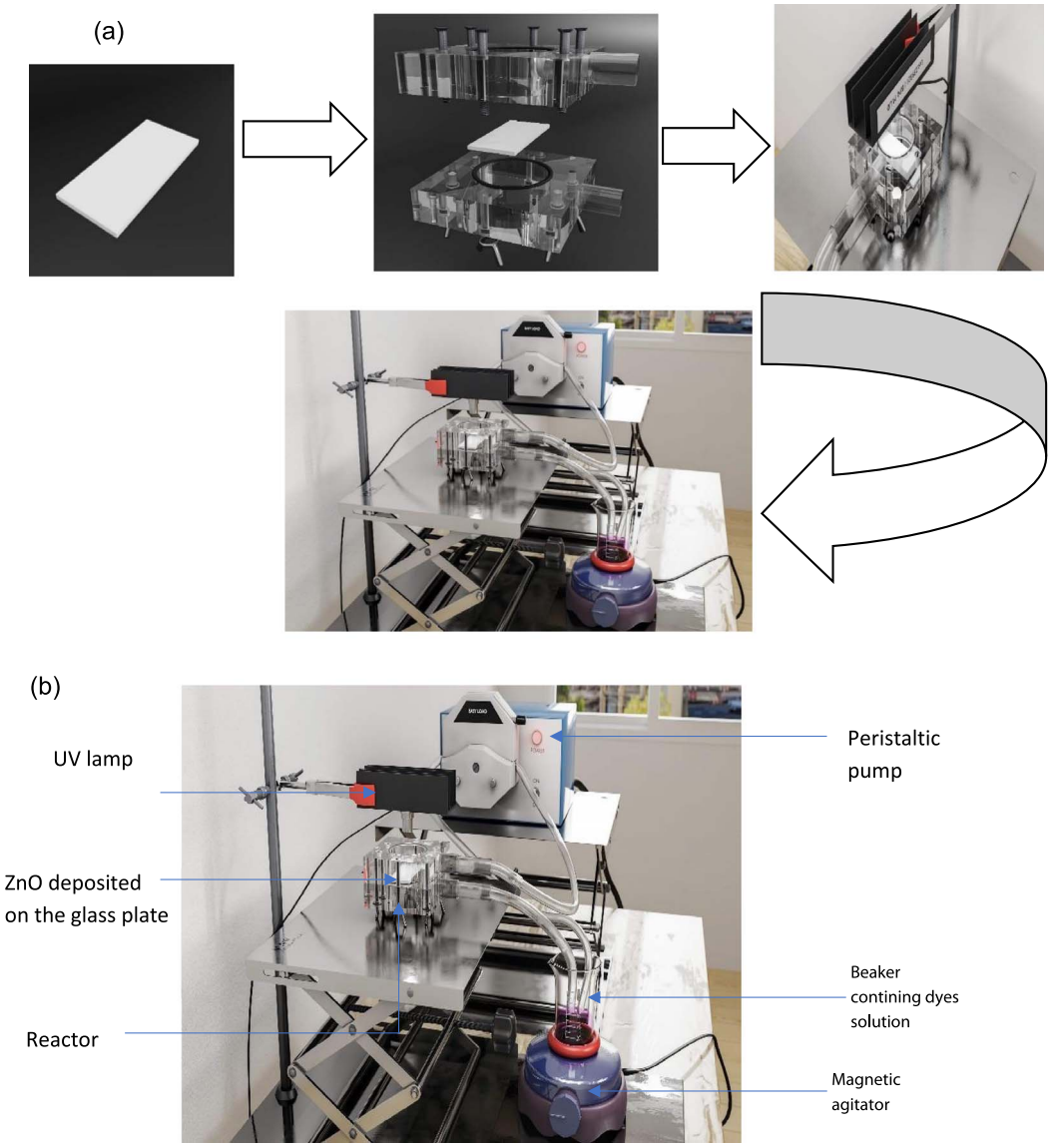

Figure 1. (a) Schematic of the pilot installation, (b) schematic for the loop photocatalytic reactor.

by the following (4):

$$\text{Yield of degradation} = \left(\frac{ABS_0 - ABS_t}{ABS_0}\right) * 100. \quad (4)$$

The kinetic constant rates K (min^{-1}) of the binary dyes mixture (RB19 + DR227) was calculated using (5) [42].

$$K * t = -Ln\left(\frac{ABS_t}{ABS_0}\right) \quad (5)$$

where ABS_0 is the initial absorbance and ABS_t is the absorbance at the instant t.

2.6.1. *Chemical oxygen demand (COD)*

COD was measured by the COD (MERCK Spectroquant TR 420) apparatus. The duration of digestion was for 120 min at 148 °C, which followed the norm ISO 15705:2002 (F). The range of COD was (0–40 $\text{mg}\cdot\text{L}^{-1}$).

2.6.2. *Biological oxygen demand (BOD_5)*

BOD_5 was measured at the initial and final experiments, in the presence of the blank for the

determination of the endogenous respiration of microorganisms. The technique was based on the manometric principle allowing the determination of the BOD_5 according to the standard NF EN 1899-2 related to the autocontrol. The value of BOD_5 was calculated from the following formula: BOD_5 = COD/1.46. The inoculum used for the BOD_5 assays was a solution of bacteria prepared as follows: 55 g of the damp earth or (50 g of the dry earth) was stirred in a 500 ml flask for 20 min. The supernatant was recuperated after decantation. The following mineral medium was used for all experiments ($g{\cdot}L^{-1}$): 22.5 $MgSO_4{\cdot}7H_2O$; 27.5 $CaCl_2$; 0.15$FeCl_3$; 2.0 NH_4Cl; 6.80 Na_2HPO_4; 2.80 KH_2PO_4. The sample to be analyzed was introduced into the Oxitop IS6 (from WTW, Alès, France) with the nutrient medium, the buffer solution, the nitrate inhibitor solution, and the bacteria solution. The pH was adjusted to a value of 7.0 ± 0.2. NaOH was placed in the rubber cap on the BOD_5 vial to absorb the released CO_2. After 5 days, the BOD_5 measurements were recorded. The obtained values were multiplied by the dilution factor to obtain the final BOD_5 value.

A control sample was run applying the same mentioned protocol of BOD_5, it consisted of a solution of easily biodegradable compounds, namely glutamic acid (150 $mg{\cdot}L^{-1}$) and glucose (150 $mg{\cdot}L^{-1}$).

2.6.3. *Phytotoxicity of germination tests on watercress seeds*

Ten filter papers were cut to the same shape as the Petri dish and placed inside ten Petri dishes. Then, moistened with (5 ml of the binary dyes mixture (RBBR + DR227). The tests were conducted using watercress seeds (*Lepidium sativum*) from the La *Semence* Bio brand, France. 10 watercress seeds were placed in each Petri dish, the whole was introduced into an oven at 25 °C for 48 h. Under the same conditions, the control sample was carried out in ten petri dishes containing 5 ml of tap water and ten watercress seeds each. The germination index (GI) was determined from the calculation of the average sprouted seeds and the average root shoots was based on the following relationships:

$$\mathrm{GI}\ (\%) = \left(\frac{\text{Seed germination (\%)} * \text{average of root length of the sample}}{\text{Seed germination (\%)} * \text{average of root length of the control}}\right) * 100. \quad (6)$$

The phytotoxicity test was conducted with watercress seeds for the treated and initial solutions of the dyes mixture.

3. Results and discussion

3.1. *Characterization of the ZnO nanostructures*

3.1.1. *X-ray diffraction (XRD), FT-IR and Raman spectra*

Figure 2(a) shows the XRD patterns of the ZnO NPs of the two samples, the 2θ peaks at 31°, 34°, 47°, 56°, 62°, 66°, 67°, 68° and 74° correspond to the reflections of reticular plans (100), (002), (101), (102), (110), (103), (200), (112), (201) and (004) of the Wurtzite structure in agreement with JCPDS card number 04-008-6994 [43–45], matched with the hexagonal symmetry (space group P63mc), which has the following lattice parameters: a = 0.3269 nm and c = 0.5203 nm [41]. No impurities or secondary phases are detected on the patterns. The narrowness of the peaks indicates a good crystallinity and demonstrates the long-range periodicity of ZnO prepared by both methods. Debye Scherer's equation (6) is used for the determination of the average crystallite size (D) of the samples using the full width at half maxima (FWHM = β) [46].

$$D = \frac{0.94\lambda}{\beta \mathrm{Cos}\,\theta} \quad (7)$$

where D—represents the size of the crystalline (nm), λ—is the incident wavelength of Cu Kα radiation X-ray (= 1.5418 nm), β—is the maximum full width and θ—indicates the diffraction angle.

The average crystallite size (D) of the nanostructures calculated based on Scherrer's equation is 27.04 nm and 11.94 nm for ZnO deposited by "Spray" and "Spray Pyrolysis" respectively. The obtained values of the average particle size (D) are smaller than those reported in the literature [27,31,34,35].

After estimating the specific surface area (Sp) of the two samples, the yielded results are equal to 1200 m^2/g and 330 m^2/g respectively for $ZnO_{\text{Spray Pyrolysis}}$ and ZnO_{Spray}, which means that the Sp of $ZnO_{\text{Spray Pyrolysis}}$ is three times higher than the Sp of ZnO_{Spray}.

Figure 2b illustrates the FT-IR spectra of both ZnO samples "Spray" and "Spray Pyrolysis". The centered band at 500 cm^{-1} belongs to ZnO. The band located at 3500 cm^{-1} corresponds to the vibration of the OH

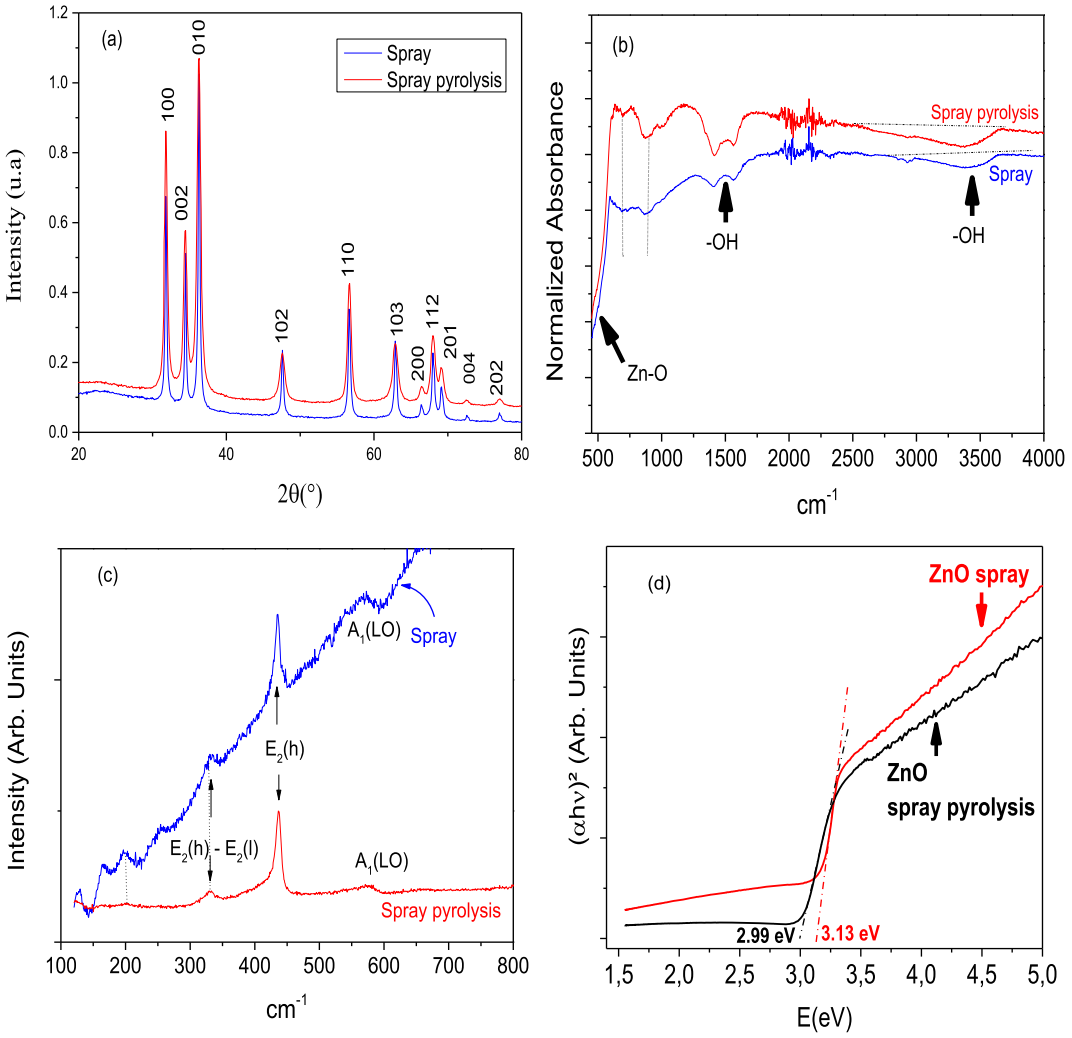

Figure 2. (a) XRD spectrum of ZnO nanoparticles, (b) the FTIR spectra of ZnO NPs, (c) Raman spectra of the ZnO films, (d) direct optical transitions of ZnO samples.

hydroxyl groups, it could also be assigned to the OH ions, which have substituted from the O_2^- ions in the structure of the compound. The centered band at about 1499 cm^{-1} is assigned to the vibration of OH ions of water molecules presented on the surface of ZnO. No traces of contaminants or impurities from the raw precursor are found in both samples. The same findings are reported elsewhere [47,48].

Based on Raman spectra, the wurtzite ZnO structure is involved and belongs to C_6V_4 (P63mc) space group with the unit cell containing 4 Zn atoms coordinated by oxygen atoms. According to the group theory, 12 normal modes are allowed by symmetry with 9 optical modes and 3 acoustic ones. The wurtzite-structured ZnO has four active Raman modes, namely, A1 + E1 + 2E2 [49,50]. Four distinct Raman peaks can be seen at 198, 331, 438, and 584 cm^{-1} (Figure 2c). The Raman peak at 331 cm^{-1} that belongs to $E_2(h) - E_2(l)$ is frequently attributed to multiple-phonon process. It signifies that the nanoparticles are single crystals [51]. The Raman peak at 438 cm^{-1} that belongs to the $E_2(h)$ mode indicates a high crystalline quality of the nanoparticles, which further confirms the formation of wurtzite ZnO [52]. The Raman peak at 584 cm^{-1} belongs to the $A_1(LO)$ mode [53].

The energy bandgap was determined from the Tauc representation:

$$\alpha h\upsilon = A(h\upsilon - E_g)^n \quad (8)$$

where α is the absorption coefficient, $h\upsilon$ is the photon energy, A is the constant, E_g is the bandgap, and $n = 1/2$ is for direct allowed transition [41,54].

The optical properties of the Spray thin ZnO film differ from those of the ZnO prepared by Spray Pyrolysis. The band gap of the as-prepared samples is found to decrease from 3.13 eV to 2.99 for ZnO prepared by Spray and Spray Pyrolysis respectively (Figure 2d).

The minor decrease in the bandgap energy of the ZnO sample synthesized by Spray Pyrolysis can also play a role in the enhancement of the photocatalytic activity [55,56]. The obtained values of the band gap energy for both samples are interesting compared to those obtained in the literature since the as-prepared materials are pure without any doping, while in the literature to obtain similar results, ZnO should be dopped with other metals to enhance the energy bandgap [55–57].

3.1.2. *Scanning electron microscopy (SEM), energy dispersive X-ray spectroscopy (EDS) and transmission electron microscopy (TEM)*

The SEM analysis shows the existence of an agglomerate of a fine powder, which forms plaques for both samples Figure 3(a, b). It is important to note that the ZnO films are regular, homogeneous and identical; and therefore, the reactivities should be the same over the entire glass plates. Moreover, the two films preparation methods give similar deposit morphologies, so the essential difference comes from the sizes and shapes of individual nanoparticles.

The EDS spectrum (EDS) reveals the presence of "Zn" and "O" peaks as shown in Figure 3(c, d). In both cases, the Zn/O ratio is close to, which is in good agreement with the previous results with.

The EDS measurements reconfirm that the prepared ZnO NPs by the two methods are pure since no residues or contaminants exist in the final nanoproduct [58].

Various ZnO nanostructures such as: nanodisks, nanowires, nanorods, nanoparticles and nanoflowers are synthesized by different techniques in the literature [59–63]. The TEM analysis reveals that ZnO nanoparticles are composed of small "spherical" particles (20 nm of average) and a small number of rods (73 nm of width and 530 nm of length of average) in the case of ZnO fixed by Spray (Figure 3e, e′). Figure 3f and f′ indicates the presence of ZnO spherical-shaped particles with a consistent size of 28 nm of average, and the absence of nanorods for ZnO fixed by Spray Pyrolysis. The same shape of ZnO prepared by Spray Pyrolysis has been observed by Sahoo *et al.*, Widiyandari *et al.* [64,65]. This finding indicates that ZnO deposited by Spray Pyrolysis has a polycrystalline character in correlation with the crystallite size calculated from DRX (11.74 nm and 28 nm for the crystallite size and the particle size respectively), While the ZnO deposited by Spray has a monocrystalline character (23 nm and 27.04 nm for the crystallite size and the particle size respectively).

3.1.3. *Electron paramagnetic resonance (RPE) and X-ray photoelectron spectroscopy (XPS)*

In the literature, the high photocatalytic activity of ZnO-NPs samples is attributed to the developed surface of aggregates (RFE) and the presence of oxygen vacancies [50], because the latter can act as electron receptors and inhibit the recombination rate of electron–hole (e^-/h^+) pairs [27]. The Oxygen vacancies can also induce band-gap narrowing and enhance visible light photocatalytic activity of ZnO [66]. An insignificant small amount of carbon impurities may induce the concomitant appearance of oxygen vacancies responsible for the green light emission evidenced by photoluminescence, as well as photocatalytic activities in the visible spectral range [67]. From Figure 4(a, b), two gyromagnetic factor "g" values are obtained considering the low and high fields of absorption peaks. The signals at $g = 1.958$, originating from VO, are observed for the elaborated materials. The signal $g = 2.0034$ is induced either by Zn interstitial or free electrons [68,69]. It is also worth mentioning that in the background spectrum there is no trace of the typical signal of carbon centered radicals (a symmetric line at $g = 2.002$) that is always present when carbon impurities are formed and left in the solid during the preparation [70]. The intensity of peaks is less important in ZnO deposited by Spray Pyrolysis.

The XPS analysis (Figure 4c) is in good agreement with the RPE and shows that the ZnO prepared by the "Spray Pyrolysis" sample has fewer oxygen

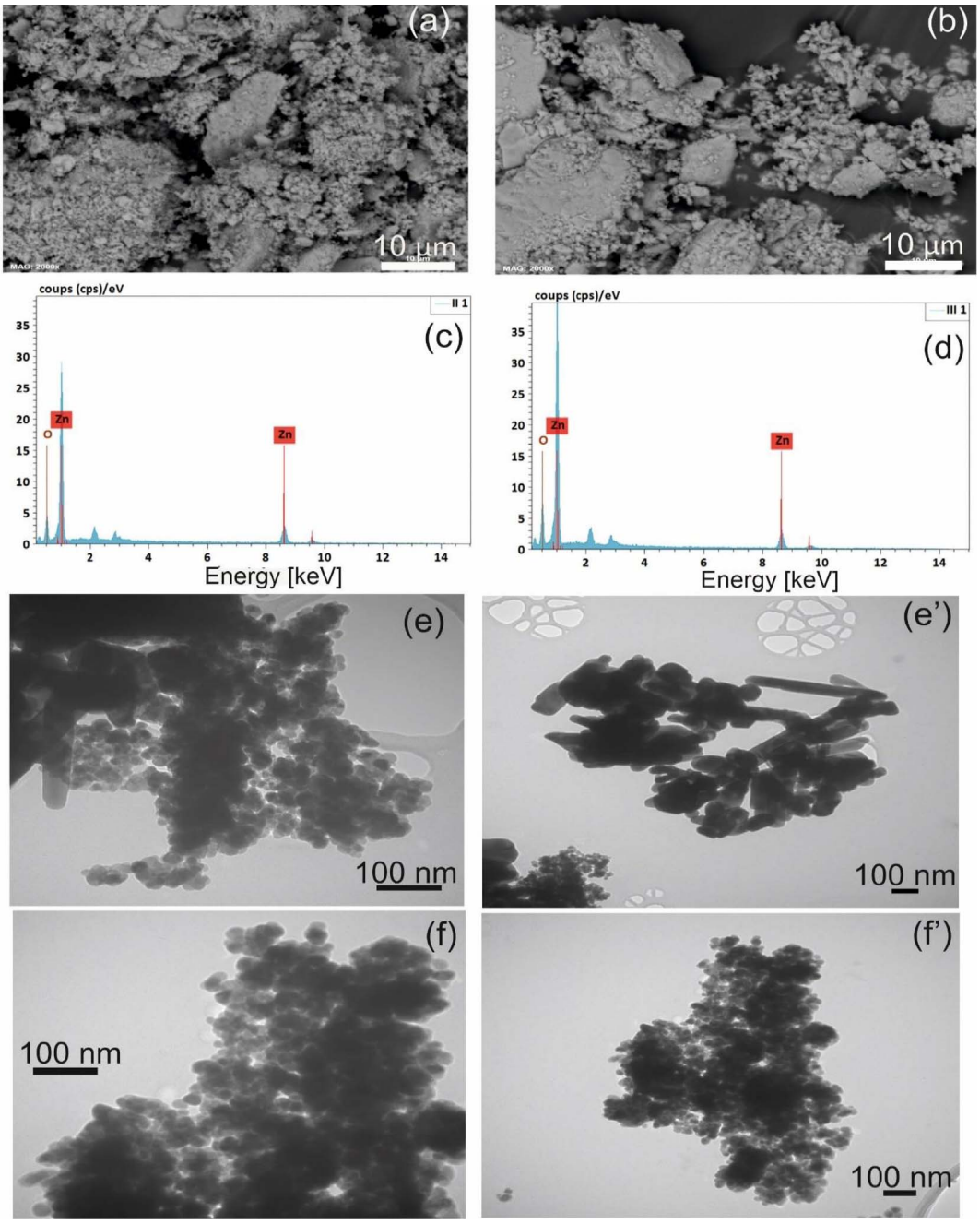

Figure 3. SEM images of ZnO nanoparticles (a) ZnO spray, (b) ZnO spray pyrolysis, the EDS spectra of ZnO nanoparticle (c) spray (d) spray pyrolysis. TEM images of ZnO nanoparticles (e, e′): ZnO spray, (f, f′) ZnO spray pyrolysis.

vacancies than ZnO "Spray". This must certainly impact the photocatalytic properties. The amount of oxygen vacancies in both samples could be assigned to the synthesis conditions, Indeed, the difference in the synthesis methods could cause the difference in oxygen vacancies.

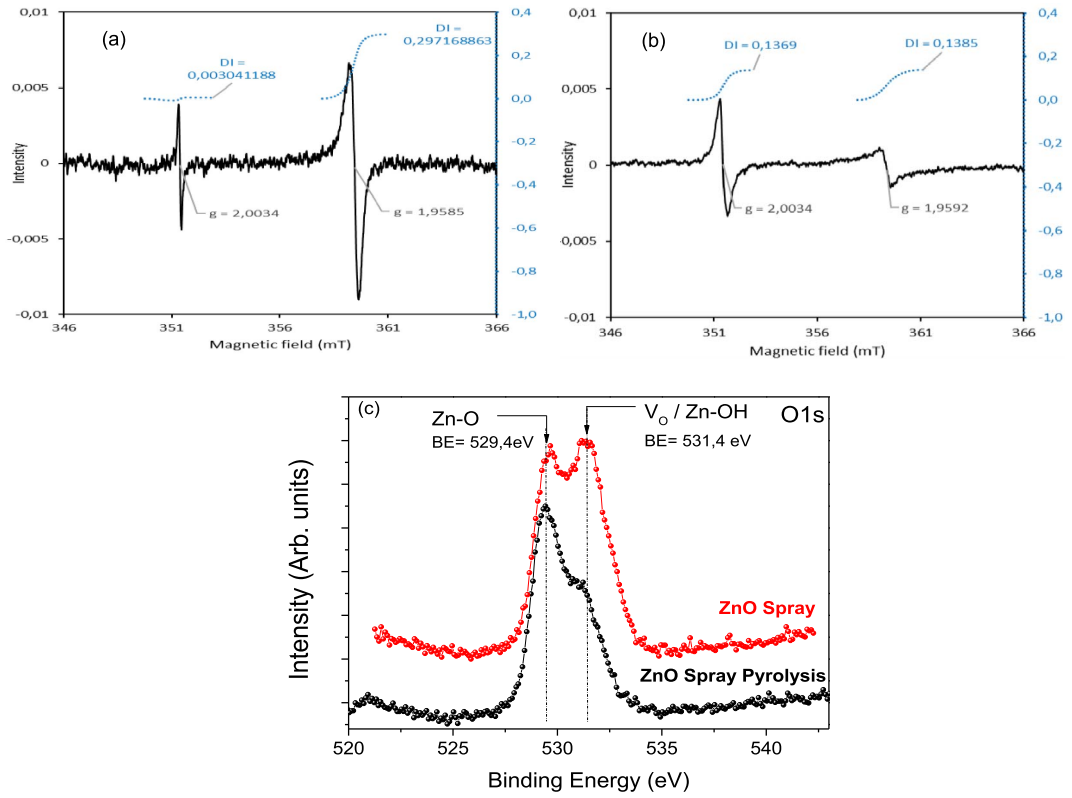

Figure 4. The RPE spectra of ZnO (a) Spray (b) Spray Pyrolysis, (c) XPS spectrum O1s.

3.2. *Photocatalytic assays*

The high photocatalytic activities of the ZnO thin films were evaluated through the degradation of the RB19 and DR227 dyes individually and in mixture under UV-light irradiation after adsorption equilibrium, as the treatment of dye mixtures is still a real challenge nowadays.

3.2.1. *Degradation of RB19 and DR 227 in single solution*

Figure 5(a) displays the adsorption capacities and photocatalytic performances of the two prepared thin films in RB19 solution under UV lamp irradiation (λ = 363 nm). The RB19 solution is quite stable under UV light irradiation without any catalysts. Experimental data indicates the absence of the adsorption capacity for the ZnO thin film prepared by Spray. Under UV-light for 390 min, the concentration of the RB19 solution reached 82% of removal yield. The reaction follows a first order kinetics, with a rate constant of 6.9×10^{-3} min^{-1} (Table 5). The ZnO thin film prepared by Spray Pyrolysis exhibits stronger adsorption capacity of RB19, which is equal to 26% indicating a slight porous structure. It presents also a better photocatalytic activity, which touched 66% with a total decolorization yield (adsoption + photocatalysis) of 92%. This confirms that the degradation of the pollutant takes place at the surface of the catalyst, the closer the pollutant is to the surface, the faster the kinetics.

Both films gave a good degradation rate; however, the thin film prepared by Spray Pyrolysis yielded better results due to the nanoparticles small size. It is highly important to note that the thin film prepared by Spray lost 12% of its initial mass, which impacts negatively the photodegradation process and explains the reason why the thin film prepared by Spray Pyrolysis showed a better photocatalytic activity. (The evaluation of the mass of the catalyst is done before and after photocatalysis using a model balance: VWRI611—3683, Type: TA314i,

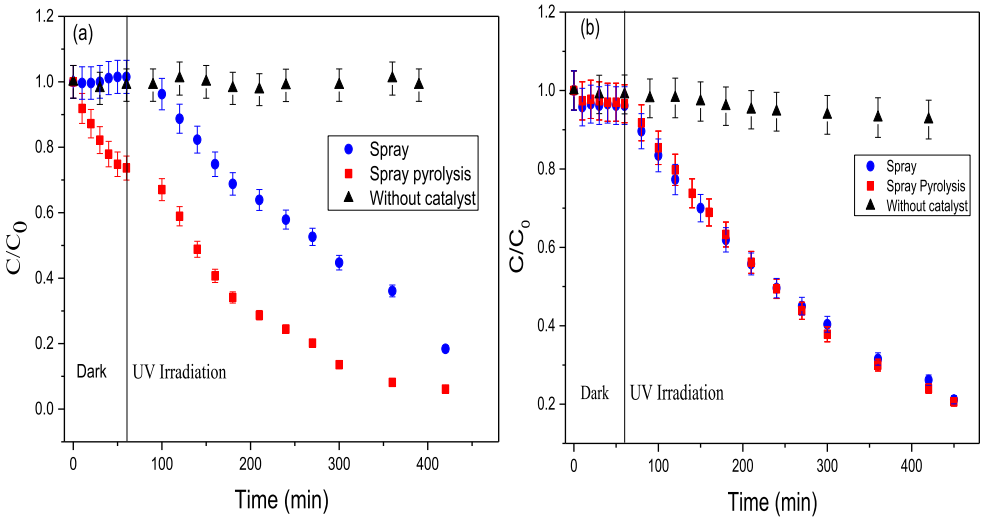

Figure 5. Evolution of the concentration during the photocatalytic process (a) RB19 ($pH_{spray\ pyrolysis}$ = 7.21, pH_{spray} = 7.26, C_0 = 10 mg·L^{-1}, P = 0.186 W), (b) DR227 ($pH_{spray\ pyrolysis}$ = 6.46, pH_{spray} = 6.83, C_0 = 10 mg·L^{-1}, P = 0.186 W).

Serial number: ITA2002546, Accuracy: 0.1 mg.) The reaction follows a first order kinetics, with a rate constant of 2.7×10^{-3} min^{-1} (Table 5).

A slight decrease in the decomposition of the DR 227 dye confirms the insufficiency of the UV irradiation to degrade this molecule (Figure 5b). The same behavior in the photocatalytic and adsorption performances is observed for the two thin films, which gave a good DR227 decolorization rate (Figure 5b). The difference in the photocatalytic behavior of the two dyes could be explained on the basis of the molar masses of the two dyes. The molar masses of the two dyes are not the same: 1.60×10^{-5} M and 5.97×10^{-6} M for RB19 and DR227 respectively. The DR227 dye has fewer chemical species in the solution than the RB19 dye, which could explain the good degradation of this molecule in the presence of the two thin layers of ZnO. The reaction follows first order kinetics, with a rate constant that equals 2.7×10^{-3} min^{-1} in case of ZnO fixed by Spray Pyrolysis. In case of ZnO immobilized by Spray, the reaction follows first order kinetics, with a rate constant of 3.2×10^{-3} min^{-1} (Table 5).

Several photocatalytic studies have demonstrated that the $^{\bullet}$OH radicals are the main oxidizing species leading to the degradation of pollutants. When a light photon falls on the surface of a semiconductor, an electron is excited and passes from the valence to the conduction band; thus, generating the electron/hole (e^-/h^+) pair. The electron reacts with dissolved oxygen to generate the superoxide radicals $O_2^{\bullet -}$, while the hole oxidizes the water molecule and/or OH^- so as to form the $OH^{\bullet}$ species. The latter is the most powerful radical found in nature since it is non-selective, i.e., it attacks all types of organic matter and converts it into simple hydrocarbons, water, and inorganic salts [56,71–73].

Even though the RB19 and DR227 pollutants belong to the families: anthraquinone and azoic dyes, the as-synthesized ZnO thin films were effective for the decomposition of the target molecules that are known by their recalcitrance and their complex molecular structure.

The residence time and the number of cycle that the liquid passes in such type of reactor is an important notion to know.

The residence time t_s in the reactor is equal to 0.833 min, calculated from the following formula:

$$Q = \frac{V}{t_s} \rightarrow t_s = \frac{V}{Q} \tag{9}$$

where: V is the volume of the solution in the reactor (L), Q: is the flow in the reactor (L·min^{-1}).

The liquid circulates 540 times in the reactor. The number of cycles (N) that the pollutant took within the reactor was calculated from the following

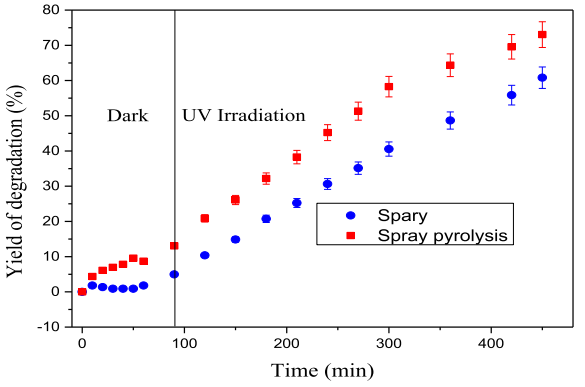

Figure 6. Evolution of the degradation rate during the photocatalytic process ($pH_{spray\ pyrolysis}$ = 7.19, pH_{spray} = 6.53, C_0 = $5_{RBBR}/5_{DR227}$ mg·L^{-1}, P = 0.186 W).

formula:

$$N = \frac{t}{t_s} \tag{10}$$

where: t: is the time of the reaction (min), t_s: is the residence time in the reactor (min).

This information is basic data that will be used for sizing a reactor in continuous mode.

3.2.2. *Mixture of the two dyes*

ZnO fixed on the glass substrate by Spray Pyrolysis reveals more superior adsorption and photocatalytic activity than the other sample (Figure 6). Moreover, its degradation efficiency reached 73% within 390 min. This could be attributed to the size of the particles that is smaller for ZnO immobilized by Spray Pyrolysis. Hence, we have opted to continue the rest of the experiments by the thin film prepared by Spray Pyrolysis. We highlight a loss of mass for ZnO prepared by Spray that is found to be 15%.

Table 4 shows the previously reported results of photocatalytic degradation of different binary organic dyes solutions in the presence of various photocatalysts.

In this study, we note a slight decrease in the removal efficiency rate of the binary mixture dyes in comparison with single aqueous dyes that might be related to the interactions between the two molecules and their by-products. Some reports highlight the enhancement in the photodegradation efficiency of the binary mixture dyes system compared with the decolorization yield of the individual dyes solutions by synergy effect [77,78].

The photodegradation of both dyes in single solution and in binary mixture follow a first order kinetic model (3) and (5). The kinetic constant rates were presented in Table 5.

The values of the kinetic rate constants K of both ZnO films for the degradation of the two dyes separately and in mixture are comparable to those already obtained in the previous studies using the same catalyst ZnO thin film prepared by other methods [57,79].

In order to optimize and enhance the decolorization rate of the mixture of the two dyes, the effect of lamp intensity and the ad of H_2O_2 will be deferred to the next sections.

3.2.3. *Effect of the light intensity and the addition of H_2O_2*

The energy saving is an important factor in the application of photocatalytic processes. The removal efficiency of the mixture of the two dyes under different UV powers of (0.093, 0.186, and 30 W) is depicted in Figure 7a. As shown, the increase in the photons flux inhibits the degradation of the dyes in mixture because at low light intensity, reactions involving (e^-/h^+) formation are principal and the recombination process is negligible. Conversely, at high light intensity, the (e^-/h^+) pair separation competes with recombination; thereby, causing a lower effect on the reaction rate [80,81].

In the goal to enhance the photocatalytic behavior of the catalyst, two different concentrations of H_2O_2 have been added to the reaction medium (Figure 7b).

Figure 7b depicts no significant effect of H_2O_2 on the decolorization of the mixture of the two dyes after addition of H_2O_2, which did not enhance the degradation rate. We note only a slight decrease in the removal rate with 12 mM H_2O_2 concentration (76% and 73% for 6 mM and 12 mM respectively). This could be traced back to the fact that the H_2O_2 molecules could exhibit a self-scavenging effect for an excess of $^{\bullet}$OH radicals; thus, leading to the formation of a perhydroxyl radical specie (HOO$^{\bullet}$), which is a less active as shown in (11) and (12). Therefore, resulting in a deterioration of the catalytic performance. This confirms the presence of (HOO$^{\bullet}$) as the most probable reactive specie that facilitates the degradation of the dyes mixture [55,82].

$$H_2O_2 + OH^{\bullet} \rightarrow H_2O + HOO^{\bullet} \tag{11}$$

$$H_2O_2 + h^+_{CB} \rightarrow H^+ + HOO^{\bullet} \tag{12}$$

Table 4. Comparison of the photocatalytic performance of different binary dyes mixture to the previous studies in the presence of various photocatalysts using mass concentrations

Catalyst		Dye1/yield of degradation (%)	Dye2/yield of degradation (%)	Mixture/yield of degradation (%)	Reference
PdTiO 0.25		100/methylene blue	100 of methyl orange	100/Binary mixture	[74]
UiO-66/$BiFeO_3$		88.7/methyl orange	89.3/of rhodamine B	84.2/Binary mixture	[75]
Cu_2SnS_3		92/rhodamine B	80/methyl orange	80	[76]
ZnO thin film	ZnO spray pyrolysis	91.86/reactive blue 19	79.40/direct red 227	73.04/Binary mixture	This work
	ZnO spray	81.57/reactive blue 19	79.02/direct red 227	60.81/Binary mixture	

Table 5. Comparison of the kinetic rate constants K of the two dyes photodegradation using both as-prepared ZnO films

Dye	Deposition method	Rate constant $K \times 10^3$ (min^{-1})	R^2
Reactive blue 19	ZnO spray pyrolysis	6.9	0.996
	ZnO spray	2.7	0.991
Direct red 227	ZnO spray pyrolysis	2.7	0.998
	ZnO spray	3.2	0.998
Binary dyes mixture	ZnO spray pyrolysis	3	0.996
	ZnO spray	2.2	0.992

The two deposition methods of ZnO on the glass plate have demonstrated similar chemical composition, structural, optical and morphological properties. Nevertheless, the ZnO prepared by Spray Pyrolysis exhibited smaller crystallite sizes which provide a larger specific surface. Indeed, this characteristic is desirable for the degradation of pollutants. ZnO fixed by both Spray and Spray Pyrolysis methods has shown good overall performances (adsorption + photocatalysis) towards the target pollutants in individual and binary mixture systems; however, the ZnO prepared by the Spray Pyrolysis method has yielded better photodegradation for RB19 dye in individual and binary mixture systems. The high light intensity has a negative impact on the performance of the photocatalytic process. Moreover, the addition of H_2O_2 has no influence on the degradation yield.

3.2.4. *Reusability and photo-stability of the catalyst for the binary dyes in mixture decolorization process*

Several reuse experiments were designed to evaluate the stability of the elaborated material. The decomposition rate remained high (74.21%) after reuse for 20 runs extending over a period of 148 h, as shown in the Figure 8(a, b).

The reproducibility of the photocatalytic experiments is confirmed and observed very clearly through the 20 photodegradion cycles. Ben Ameur *et al.* [83] have conducted many cycles of thin film of ZnO: Co (1%) doped ZnO (CZO), and In (1%) doped ZnO (IZO). Their measurements clearly showed that after three cycles, the photo-degradation remains almost constant with a deactivation not exceeding (11%). Ravichandran *et al.* [84] have investigated the photostability and reusability of ZnO:Mo/rGO as a photocatalyst. The photodegradation experiments were carried out for four cycles. Even after the fourth run, the deposited photocatalyst was found to have the degradation efficiency of about 90% and 68% within 120 min for Methylene Blue and Rhodamine B dyes respectively. Compared with previous research studies, the present thin film of ZnO fixed by Spray Pyrolysis is among the highest stable materials. This high stability after repeated usage provided the possibility for long term applications.

The before and after diffractograms cycles are very similar (Figure 8c). The ZnO material deposited on the plate did not degrade or change during the

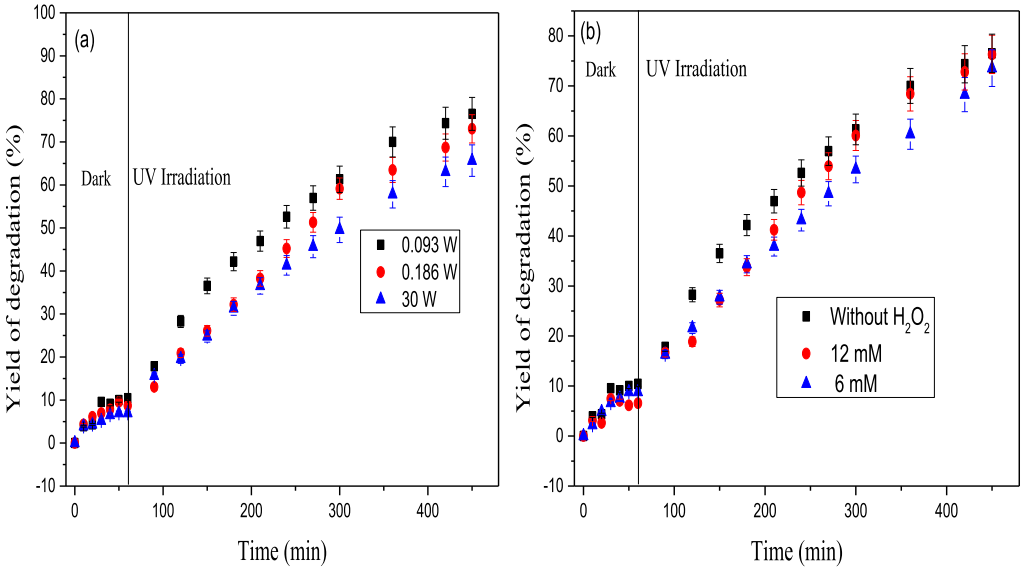

Figure 7. (a) Evolution of the degradation rate during the photocatalytic process: effect of light intensity ($pH_{30\ W}$ = 7.19, $pH_{0,186\ W}$ = 6.37, $pH_{9,2\times10^{-2}\ W}$ = 7.11, $C_0 = 5_{RBBR}/5_{DR227}$ mg·L^{-1}), (b) evolution of the degradation rate during the photocatalytic process: effect of the addition of H_2O_2 ($pH_{6\ mM}$ = 6.73, $pH_{12\ mM}$ = 7.01, $C_0 = 5_{RB19}/5_{DR227}$ mg·L^{-1}, P = 0.093 W).

20 cycles of photocatalysis. The material acted well as a catalyst.

3.3. *Biodegradability and phytotoxicity studies*

The ratio within the biological oxygen demand over 5 days (BOD_5) and the chemical oxygen demand (COD) indicates the level of the biodegradability of a sample. The ratio BOD_5/COD between $0.4 < BOD_5/COD < 1$ indicates a good biodegradability, which signifies that the sample can be easily treated by activated sludge. In our case, the biodegradability BOD_5/COD of the binary dye mixture before treatment was 0.059, which means that the mixture of dyes is non-biodegradable by microorganisms. The final solution exhibits a high ratio of BOD_5/COD that equals 0.833, which indicates that the final sample is biodegradable. Similar results are reported through the literature [85–87].

The initial mixture of dyes exhibits a moderate phytotoxicity with watercress seeds as shown in Figure 9. After the photocatalytic process, there is an absence of phytotoxicity in the treated solution, which reveals the efficiency of the treatment for reducing the toxicity of the target pollutants.

Naraginti *et al.* [88] have studied the phytotoxicity of an antibiotic sulphamethoxazole (SMX) and the azo-dye reactive-red-194 (RR194) before and after photocatalysis. The tests have demonstrated a lower percentage of germination in *Phaseolus vulgaris* (40%), *Vigna radiata* (30%) and *Phaseolus lunatus* (30%) of the seeds treated with 50 ppm of SMX, compared with the seeds treated with the degradation products (100%). The results with 50 mg·L^{-1} of RR-194 have shown as well a lower percentage of germination in *P. vulgaris* (40%), *V. radiata* (50%) and *P. lunatus* (30%) compared with the degradation products (100%). Saratale *et al.* [89] have examined the phytotoxicity before and after the photodegradation treatment of Reactive Green 19A (RG19A) and textile effluent using *Phaseolus mungo* and *Sorghum vulgare*. The results have uncovered that the products generated after the photocatalytic degradation of RG19A and textile effluent are less toxic in nature.

4. Conclusion

In summary, ZnO nanocrystalline thin films were prepared on glass substrates by two techniques namely the Spray and Spray Pyrolysis. The prepared

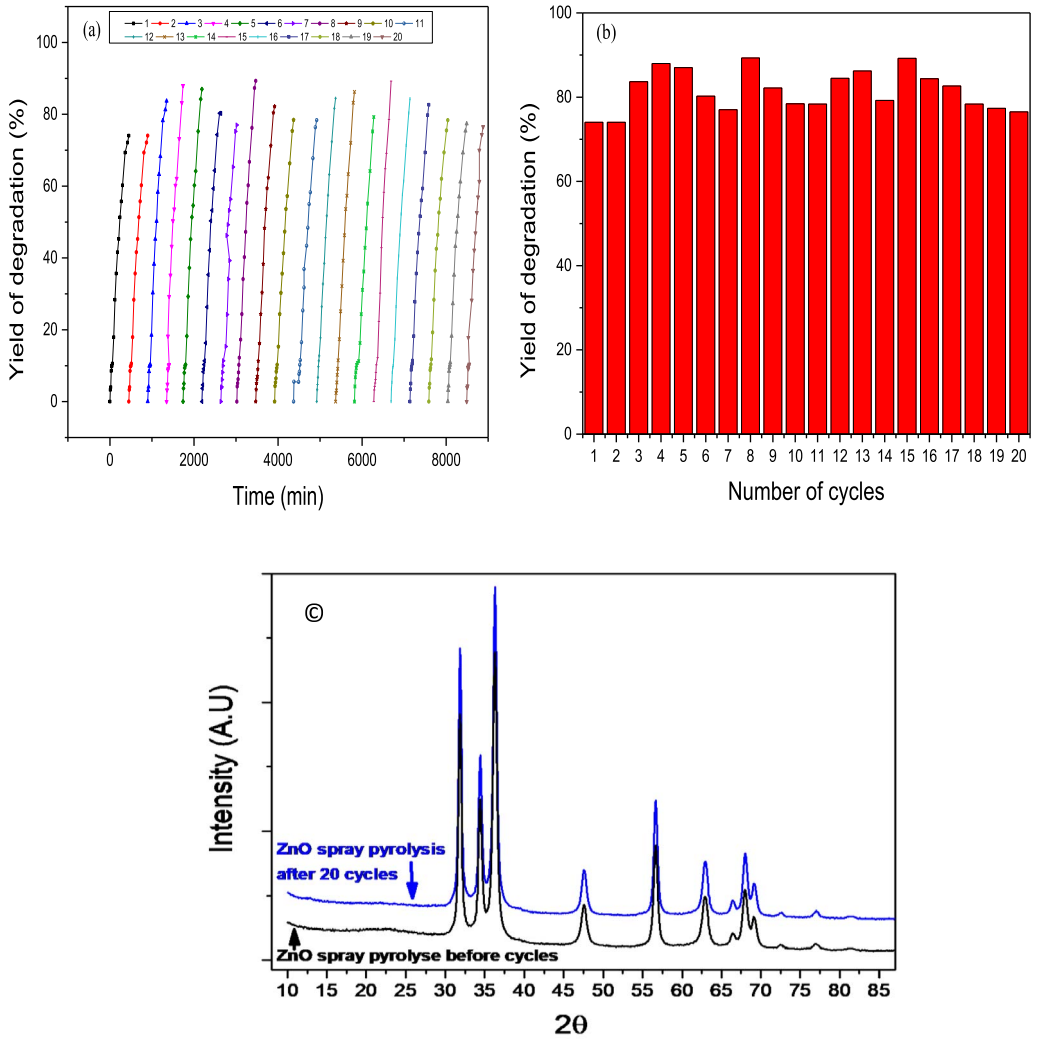

Figure 8. Cycling curves of the photocatalytic degradation of the binary dyes mixture in presence of the ZnO thin film prepared by Spray pyrolysis (P = 0.093 W), (a) kinetic curves, (b) number of cycles b, (c) XRD spectrum of ZnO nanoparticles before and after 20 photodegradation cycles.

ZnO nanoparticles were indexed to the hexagonal wurtzite ZnO polymorph. XRD and Raman were used to examine the crystal structure. The grain size and the surface morphology were analyzed by SEM and TEM. The optical properties of the ZnO films were also studied. No impurities were detected in both samples confirmed by EDX and FT-IR. ZnO deposited by Spray contains more oxygen vacancies evaluated by EPR and XPS. The ZnO thin films prepared by Spray Pyrolysis showed a better photocatalytic performance compared with the other sample (73% and 61% respectively for ZnO deposited by Spray Pyrolysis and Spray). This photocatalytic activity can be explained based on the smaller size of the crystallites and nanoparticles of the material on one hand and the lower energy of the band gap on the other hand. The elaborated material exhibited a high photostability even after 20 cycles of reutilization (148 h). BOD_5/COD rate enhanced from 0.053 to 0.83 showing better biodegradability of the treated solution. The germination phytotoxicity test has improved from 75% to 100%.

This study reports an economic and ecofriendly decolorization process that may open an interesting

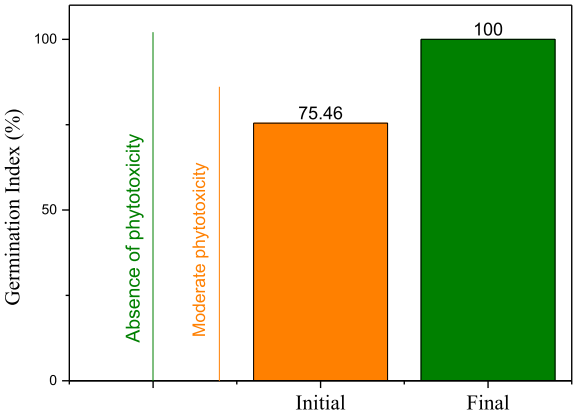

Figure 9. Phytotoxicity test of the binary dyes mixture before and after photocatalytic degradation (C_0 = $5_{RB19}/5_{DR227}$ mg·L^{-1}, P = 0.093 W).

route to achieve a high efficiency of the photocatalytic activity through the immobilized ZnO dedicated to the effluent treatment on a semi-pilot scale.

Conflicts of interest

The authors declare that they have no known competing financial interests or personal relationships that could have appeared to influence the work reported in this paper.

Acknowledgments

The authors thank Ivane Lelievre (Unilasalle-EME) for her technical help, the English language teacher Souad Cherif for her helpful English revision, the Centre Imagerie Cellulaire Sante (Clermont Auvergne University), most notably Christelle Blavignac, for her technical assistance in TEM analysis and the Framework of the LabEx IMobS^3, Guillaume Monier of Institut Pascal (UMR 6602) for his technical assistance in XPS measure, Pr. Daniel Zambon and Dr. Angélique Bousquet from ICCF and the Algerian Ministry of Higher Education and Scientific Research for its offer of the PNE scholarship that allowed to finance the scientific training in France.

References

[1] A. Maroudas, P. K. Pandis, A. Chatzopoulou, L. R. Davellas, G. Sourkouni, C. Argirusis, *Ultrason. Sonochem.*, 2021, **71**, article no. 105367.

[2] S. Dursun, S. N. Koyuncu, İ. C. Kaya, G. G. Kaya, V. Kalem, H. Akyildiz, *J. Water Process Eng.*, 2020, **36**, article no. 101390.

[3] T. R. Waghmode, M. B. Kurade, R. T. Sapkal, C. H. Bhosale, B. H. Jeon, S. P. Govindwar, *J. Hazard. Mater.*, 2019, **371**, 115-122.

[4] S. Cherif, H. Rezzaz-Yazid, Z. Sadaoui, M. Trari, *J. Water Chem. Technol.*, 2021, **43**, 164-172.

[5] D. D. La, C. V. Tran, N. T. T. Hoang, M. D. Doan Ngoc, T. H. P. Nguyen, H. T. Vo, P. H. Ho, T. A. Nguyen, S. V. Bhosale, X. C. Nguyen, S. W. Chang, W. J. Chung, D. D. Nguyen, *Fuel*, 2020, **281**, article no. 118655.

[6] J. M. Herrmann, J. Disdier, M. N. Mozzanega, P. Pichat, *J. Catal.*, 1979, **60**, 369-377.

[7] O. Baaloudj, H. Kenfoud, A. K. Badawi, A. A. Assadi, A. El Jery, A. A. Assadi, A. Amrane, *Catal. MDPI*, 2022, **12**, article no. 500.

[8] A. Tab, B. Bellal, C. Belabed, M. Dahmane, M. Trari, *Optik (Stuttg)*, 2020, **214**, article no. 164858.

[9] O. Baaloudj, I. Assadi, N. Nasrallah, A. El Jery, L. Khezami, A. A. Assadi, *J. Water Process Eng.*, 2021, **42**, article no. 102089.

[10] O. Baaloudj, N. Nasrallah, R. Bouallouche, H. Kenfoud, L. Khezami, A. A. Assadi, *J. Clean. Prod.*, 2022, **330**, article no. 129934.

[11] O. Baaloudj, H. Nasrallah, N. Kenfoud, F. Algethami, A. Modwi, A. Guesmi, L. Assadi, A. A. Khezami, *Materials (Basel)*, 2021, **14**, article no. 5409.

[12] H. Kenfoud, O. Baaloudj, N. Nasrallah, R. Bagtache, A. A. Assadi, M. Trari, *J. Mater. Sci. Mater. Electron.*, 2021, **32**, 16411-16420.

[13] H. Zeghioud, A. A. Assadi, N. Khellaf, H. Djelal, A. Amrane, S. Rtimi, *Materials (Basel)*, 2019, **12**, article no. 412.

[14] N. Li, R. Li, J. Zhao, L. Liang, Y. Yu, L. Kong, G. Chen, B. Yan, *Chem. Eng. J.*, 2020, **394**, article no. 124997.

[15] A. Di Mauro, C. Farrugia, S. Abela, P. Refalo, M. Grech, L. Falqui, V. Privitera, G. Impellizzeri, *Mater. Sci. Semicond. Process.*, 2020, **118**, article no. 105214.

[16] M. L. Tran, C. C. Fu, L. Y. Chiang, C. Te Hsieh, S. H. Liu, R. S. Juang, *J. Environ. Chem. Eng.*, 2020, **8**, article no. 104422.

[17] C. M. Taylor, D. Mattia, J. Wenk, *J. Environ. Chem. Eng.*, 2020, **8**, article no. 103798.

[18] F. C. S. M. R. Lopes, M. da G. C. da Rocha, P. Bargiela, H. Sousa Ferreira, C. A. de M. Pires, *Chem. Eng. Sci.*, 2020, **227**, article no. 115939.

[19] S. Sandhu, S. Krishnan, A. V. Karim, A. Shriwastav, *J. Environ. Chem. Eng.*, 2020, **8**, article no. 104471.

[20] J. J. Alvear-Daza, D. Pais-Ospina, D. A. Marín-Silva, A. Pinotti, L. Damonte, L. R. Pizzio, P. Osorio-Vargas, J. A. Rengifo-Herrera, *Catal. Today*, 2020, **372**, 11-19.

[21] O. Ounas, B. Lekhlif, J. Jamal-Eddine, *Mater. Today Proc.*, 2019, **30**, 816-822.

[22] J. Liu, Y. Zhao, J. Ma, Y. Dai, J. Li, J. Zhang, *Ceram. Int.*, 2016, **42**, 15968-15974.

[23] A. Khataee, M. Kıranşan, S. Karaca, M. Sheydaei, *J. Taiwan Inst. Chem. Eng.*, 2017, **74**, 196-204.

[24] O. Sacco, V. Vaiano, M. Matarangolo, *Sep. Purif. Technol.*, 2018, **193**, 303-310.

[25] H. Mahdizadeh, A. Nasiri, M. A. Gharaghani, G. Yazdanpanah, *MethodsX*, 2020, **7**, article no. 101118.

[26] S. Deebansok, T. Amornsakchai, P. Sae-Ear, P. Siriphannon, S. M. Smith, *J. Environ. Chem. Eng.*, 2021, **9**, article no. 104746.

[27] M. Malakootian, M. Khatami, H. Mahdizadeh, A. Nasiri, M. Amiri Gharaghani, *Inorg. Nano-Metal Chem.*, 2020, **50**, 124-135.
[28] T. Aissani, I. Yahiaoui, F. Boudrahem, L. Yahia Cherif, F. Fourcad, A. Amrane, F. Aissani-Benissad, *React. Kinet. Mech. Catal.*, 2020, **131**, 471-487.
[29] S. Singh, H. Mahalingam, P. K. Singh, *Appl. Catal. A Gen.*, 2013, **462–463**, 178-195.
[30] A. J. Jafari, R. R. Kalantari, M. Kermani, M. H. Firooz, *Chem. Pap.*, 2019, **73**, 635-644.
[31] N. Yudasari, D. S. Kennedy, M. M. Suliyanti, *J. Phys. Conf. Ser.*, 2019, **1191**, article no. 012009.
[32] K. Kaviyarasu, C. Maria Magdalane, K. Kanimozhi, J. Kennedy, B. Siddhardha, E. Subba Reddy, N. K. Rotte, C. S. Sharma, F. T. Thema, D. Letsholathebe, G. T. Mola, M. Maaza, *J. Photochem. Photobiol. B Biol.*, 2017, **173**, 466-475.
[33] H. K. Hakki, S. Allahyari, N. Rahemi, M. Tasbihi, *C. R. Chim.*, 2019, **22**, 393-405.
[34] V. Mata, A. Maldonado, M. de la Luz Olvera, *Mater. Sci. Semicond. Process.*, 2018, **75**, 288-295.
[35] I. Loyola Poul Raj, A. Jegatha Christy, R. David Prabu, N. Chidhambaram, M. Shkir, S. AlFaify, A. Khan, *Inorg. Chem. Commun.*, 2020, **119**, article no. 108082.
[36] A. Henni, N. Harfouche, A. Karar, D. Zerrouki, F. X. Perrin, F. Rosei, *Solid State Sci.*, 2019, **98**, article no. 106039.
[37] O. Tokode, R. Prabhu, L. A. Lawton, P. K. J. Robertson, *J. Environ. Chem. Eng.*, 2017, **5**, 3942-3948.
[38] P. Bansal, A. Verma, *J. Clean. Prod.*, 2018, **195**, 540-551.
[39] I. Y. Habib, J. Burhan, F. Jaladi, C. M. Lim, A. Usman, N. T. R. N. Kumara, S. C. E. Tsang, A. H. Mahadi, *Catal. Today*, 2021, **375**, 506-513.
[40] M. R. Sohrabi, M. Ghavami, *Desalination*, 2010, **252**, 157-162.
[41] S. Cherif, H. Yazid, G. Rekhila, Z. Sadaoui, M. Trari, *Optik (Stuttg)*, 2021, **238**, article no. 166751.
[42] M. Ismail, Z. Wu, L. Zhang, J. Ma, Y. Jia, Y. Hu, Y. Wang, *Chemosphere*, 2019, **228**, 212-218.
[43] M. C. Uribe-López, M. C. Hidalgo-López, R. López-González, D. M. Frías-Márquez, G. Núñez-Nogueira, D. Hernández-Castillo, M. A. Alvarez-Lemus, *J. Photochem. Photobiol. A Chem.*, 2021, **404**, article no. 112866.
[44] R. Shashanka, H. Esgin, V. M. Yilmaz, Y. Caglar, *J. Sci. Adv. Mater. Devices*, 2020, **5**, 185-191.
[45] E. Vidhya, S. Vijayakumar, S. Prathipkumar, P. K. Praseetha, *Gene Rep.*, 2020, **20**, article no. 100688.
[46] A. Awasthi, P. Sharma, L. Jangir, Kamakshi, G. Awasthi, K. K. Awasthi, K. Awasthi, *Mater. Sci. Eng. C*, 2020, **113**, article no. 111021.
[47] W. Lopes de Almeida, N. S. Ferreira, F. S. Rodembusch, V. Caldas de Sousa, *Mater. Chem. Phys.*, 2021, **258**, article no. 123926.
[48] C. Rodwihok, K. Charoensri, D. Wongratanaphisan, W. M. Choi, S. H. Hur, H. J. Park, J. S. Chung, *J. Mater. Sci. Technol.*, 2021, **76**, 1-10.
[49] L. Lima, L. de S. Caldas, A. Alí, J. Barreto, R. Freitas, A. Mazzarella, G. Felix, V. Carozo, F. Stavale, *Surf. Sci.*, 2021, **704**, article no. 121748.
[50] R. L. de S. e. Silva, A. Franco, *Mater. Sci. Semicond. Process*, 2020, **119**, article no. 105227.
[51] B. S. Mwankemwa, F. J. Nambala, F. Kyeyune, T. T. Hlatshwayo, J. M. Nel, M. Diale, *Mater. Sci. Semicond. Process*, 2017, **71**, 209-216.
[52] P. Sharma, N. Kumar, R. Chauhan, V. Singh, V. C. Srivastava, R. Bhatnagar, *Chem. Eng. J.*, 2020, **392**, article no. 123746.
[53] C. C. Wang, F. S. Shieu, H. C. Shih, *J. Environ. Chem. Eng.*, 2021, **9**, article no. 104707.
[54] S. Wannapop, A. Khawsaad, A. Supanpong, Y. Janorat, Y. Chuminjak, A. Tuantranont, A. Phuruangrat, T. Thongtem, S. Thongtem, A. Somdee, *Inorg. Chem. Commun.*, 2022, **138**, article no. 109210.
[55] A. Mohammadzadeh, M. Khoshghadam-Pireyousefan, B. Shokrianfard-Ravasjan, M. Azadbeh, H. Rashedi, M. Dibazar, A. Mostafaei, *J. Alloys Compd.*, 2020, **845**, article no. 156333.
[56] D. S. Vasanthi, K. Ravichandran, P. Kavitha, S. Sriram, P. K. Praseetha, *Superlattices Microstruct.*, 2020, **145**, article no. 106637.
[57] A. Omerzu, R. Peter, D. Jardas, I. Turel, K. Salamon, M. Podlogar, D. Vengust, I. Jelovica Badovinac, I. Kavre Piltaver, M. Petravic, *Surf. Interfaces*, 2021, **23**, article no. 100984.
[58] Q. K. Doan, M. H. Nguyen, C. D. Sai, V. T. Pham, H. H. Mai, N. H. Pham, T. C. Bach, V. T. Nguyen, T. T. Nguyen, K. H. Ho, T. H. Tran, *Appl. Surf. Sci.*, 2020, **505**, article no. 144593.
[59] F. U. Khan, Z. U. H. Khan, J. Ma, A. U. Khan, M. Sohail, Y. Chen, Y. Yang, X. Pan, *Mater. Sci. Eng. C*, 2021, **118**, article no. 111432.
[60] S. Rajamanickam, S. M. Mohammad, Z. Hassan, *Colloids Interface Sci. Commun.*, 2020, **38**, article no. 100312.
[61] Y. Wang, H. Xu, G. Zan, T. Wu, Q. Wu, *Chemosphere*, 2020, **259**, article no. 127292.
[62] D. Zhao, W. Liu, G. Zhu, Y. Zhang, Y. Wang, W. Zhou, C. Xu, S. Xie, B. Zou, *Nano Energy*, 2020, **78**, article no. 105202.
[63] T. Zaheer, M. Imran, K. Pal, M. S. Sajid, R. Z. Abbas, A. I. Aqib, M. A. Hanif, S. R. Khan, M. K. Khan, Z. ud D. Sindhu, S. ur Rahman, *J. Mol. Struct.*, 2021, **1227**, article no. 129652.
[64] B. Sahoo, S. K. Pradhan, D. K. Mishra, S. K. Sahoo, R. R. Nayak, D. Behera, *Optik (Stuttg)*, 2021, **228**, article no. 166134.
[65] H. Widiyandari, S. Wijayanti, A. Prasetio, A. Purwanto, *Opt. Mater. (Amst)*, 2020, **107**, article no. 110077.
[66] X. Rong, F. Qiu, J. Rong, X. Zhu, J. Yan, D. Yang, *Mater. Lett.*, 2016, **164**, 127-131.
[67] V. N. Krasil'nikov, T. V. Dyachkova, A. P. Tyutyunnik, O. I. Gyrdasova, M. A. Melkozerova, I. V. Baklanova, Y. A. Perevozchikova, S. M. Emelyanova, H. W. Weber, V. V. Marchenkov, *Mater. Res. Bull.*, 2018, **97**, 553-559.
[68] Z. Remes, M. Buryi, N. Neykova, J. Stuchlik, J. Micova, H. S. Hsu, *Mater. Today Proc.*, 2020, **33**, 2481-2483.
[69] Q. Sun, T. Tian, L. Zheng, Z. Man, G. Li, M. Barré, J. Dittmer, A. Bulou, A. H. Kassiba, *J. Eur. Ceram. Soc.*, 2019, **39**, 3070-3076.
[70] E. Cerrato, M. C. Paganini, E. Giamello, *J. Photochem. Photobiol. A Chem.*, 2020, **397**, article no. 112531.
[71] S. Ibrahim, P. Bonnet, M. Sarakha, C. Caperaa, G. Monier, A. Bousquet, *Mater. Chem. Phys.*, 2020, **243**, article no. 122580.
[72] W. Lou, A. Kane, D. Wolbert, S. Rtimi, A. A. Assadi, *Chem. Eng. Process. Process Intensif.*, 2017, **122**, 213-221.
[73] H. Zeghioud, A. A. Assadi, N. Khellaf, H. Djelal, A. Amrane, S. Rtimi, *J. Photochem. Photobiol. A Chem.*, 2018, **365**, 94-102.
[74] C. H. Nguyen, C. C. Fu, R. S. Juang, *J. Clean. Prod.*, 2018, **202**, 413-427.

[75] S. Bargozideh, M. Tasviri, S. Shekarabi, H. Daneshgar, *New J. Chem.*, 2020, **44**, 13083-13092.
[76] M. B. Zaman, R. Poolla, *Opt. Mater. (Amst)*, 2020, **104**, article no. 109853.
[77] S. Sharma, N. Khare, *Adv. Powder Technol.*, 2018, **29**, 3336-3347.
[78] S. Wang, F. Teng, Y. Zhao, *RSC Adv.*, 2015, **5**, 76588-76598.
[79] J. P. C. Moura, R. Y. N. Reis, A. E. B. Lima, R. S. Santos, G. E. Luz, *J. Photochem. Photobiol. A Chem.*, 2020, **401**, article no. 112778.
[80] M. N. Rashed, *Int. J. Phys. Sci.*, 2007, **2**, 73-81.
[81] G. Alhakimi, L. H. Studnicki, M. Al-Ghazali, *J. Photochem. Photobiol. A Chem.*, 2003, **154**, 219-228.
[82] A. M. A. Abdelsamad, T. A. Gad-Allah, F. A. Mahmoud, M. I. Badawy, *J. Water Process Eng.*, 2018, **25**, 88-95.
[83] S. Ben Ameur, H. BelHadjltaief, B. Duponchel, G. Leroy, M. Amlouk, H. Guermazi, S. Guermazi, *Heliyon*, 2019, **5**, article no. e01912.
[84] K. Ravichandran, C. Dhanraj, M. Mohamed Ibrahim, P. Kavitha, *Mater. Today Proc.*, 2020, **48**, 234-244.
[85] A. Arques, A. M. Amat, A. García-Ripoll, R. Vicente, *J. Hazard. Mater.*, 2007, **146**, 447-452.
[86] A. S. Anjana Anand, S. Adish Kumar, J. Rajesh Banu, G. Ginni, *Desalin. Water Treat.*, 2016, **57**, 8236-8242.
[87] D. Salazar-Beltrán, L. Hinojosa-Reyes, F. Maya-Alejandro, G. Turnes-Palomino, C. Palomino-Cabello, A. Hernández-Ramírez, J. L. Guzmán-Mar, *Photochem. Photobiol. Sci.*, 2019, **18**, 863-870.
[88] S. Naraginti, Y. Li, G. L. Puma, *Ecotoxicol. Environ. Saf.*, 2018, **159**, 301-309.
[89] R. G. Saratale, G. S. Ghodake, S. K. Shinde, S. K. Cho, G. D. Saratale, A. Pugazhendhi, R. N. Bharagava, *J. Environ. Manage.*, 2018, **223**, 1086-1097.